Study of the tetragonal-to-cubic phase transition in $PbTiO_3$ nanopowders

2006 J. Phys.: Condens. Matter 18 3861

(http://iopscience.iop.org/0953-8984/18/15/028)

INSTITUTE OF PHYSICS PUBLISHING JOURNAL OF PHYSICS: CONDENSED MATTER

J. Phys.: Condens. Matter **18** (2006) 3861–3874 doi:10.1088/0953-8984/18/15/028

Study of the tetragonal-to-cubic phase transition in $PbTiO_3$ nanopowders

Emre Erdem[1], Hans-Christoph Semmelhack[1], Rolf Böttcher[1], Holger Rumpf[2], Juras Banys[3], Anke Matthes[4], Hans-Jürgen Gläsel[4], Dietmar Hirsch[4] and Eberhard Hartmann[4]

[1] Institut für Experimentelle Physik II, Universität Leipzig, D-04103 Leipzig, Germany
[2] Center of Advanced European Studies and Research (*caesar*), D-53175 Bonn, Germany
[3] Faculty of Physics, Vilnius University, 10222 Vilnius, Lithuania
[4] Leibniz-Institut für Oberflächenmodifizierung, D-04303 Leipzig, Germany

E-mail: hartmann@uni-leipzig.de

Received 6 January 2006
Published 30 March 2006
Online at stacks.iop.org/JPhysCM/18/3861

Abstract

The CPP (combined polymerization and pyrolysis) preparation route, in its enhanced liquid-precursor-based version, was combined with consecutive soft milling. For studies of temperature- and size-dependent structural changes occurring in ferroelectric lead titanate, this combined route yields a nanopowder series covering the relevant particle-size region at target quality. This material basis enables consistent SEM, TEM, XRD, Raman, EPR and dielectric measurements, which furnish a comprehensive picture of the cooperation between temperature rise and size reduction to eliminate tetragonality and concomitant ferroelectricity. Our previous original EPR studies on nanosized barium titanate are now extended to the lead titanate case. Furthermore, as compared to the pertinent literature standard, the materials basis is extended to powder samples of smaller mean particle sizes, comprising the critical size at which a $PbTiO_3$ particle undergoes a transition into cubic paraelectric phase. Thus, the size-driven phase transition can be observed in a direct way (at 7 nm, which compares to 40 nm for $BaTiO_3$), and the EPR data suggest a much less spacious gradient shell at the particle surfaces (thickness $\approx$ 2 nm) than in previous analogous investigations on $BaTiO_3$ (15 nm).

1. Introduction

Thanks to growing technological applications, size effects in ferroelectric nanoparticles have obtained great impetus in recent years [1, 2]. Relevant parameters such as Curie temperature, spontaneous polarization, coercive field, switching speed etc depend on the mean particle size and the size distribution function in the thin films and powder samples. For discussing these size effects, several models have been proposed, which take into account the surface

boundary conditions comprising surface relaxation [3, 4] and polarization [5, 6]. In early literature [7], size effects are based on a core–shell model of ferroelectric nanoparticles where the core is tetragonal and the shell is cubic. In recent studies of size effects occurring in $BaTiO_3$ nanopowders [8], in a close correspondence with analogous thin film studies [2, 3], the homogeneous surface shell was urgently replaced by a tetragonal-to-cubic gradient layer. In this paper, such a core–shell idea with gradient surface layer is maintained, with the focus mainly set on the phenomenology of the temperature and size effects. The original data are then amenable to due classification by pertinent theoreticians. In addition, a methodological aspect is worth mentioning: Müller *et al* [9] demonstrated the great potential of the electron paramagnetic resonance (EPR) spectroscopic method to furnish information on the local structure of perovskitic bulk material. This approach also proved exceedingly efficient in studying Mn and Cr doped $BaTiO_3$ bulk systems [10, 11]. Hence, it seemed promising to extend this approach to nano-sized ferroelectric material (for nano-$BaTiO_3$:Mn^{2+}, see [8]) and, indeed, the parameters of the core–shell model could be determined quantitatively. To apply the EPR-based methodological pattern now to chromium-doped $PbTiO_3$ nanopowder is not just a simple retake of previous work on $BaTiO_3$:Mn^{2+} [8]. In $PbTiO_3$, the outer Pb 6s electrons are involved in the much stronger covalent bonding, thus imposing a more stable ferroelectricity on $PbTiO_3$ than on $BaTiO_3$, which becomes manifest by e.g. greater spontaneous polarization and higher Curie temperature. Obviously, one may also expect that the 6s binding peculiarity of $PbTiO_3$ also translates in a rather different phenomenology of size and temperature driven tetragonal-to-cubic phase transition. In the present study stress is laid on this particular phenomenology.

In experimental studies of size effects and particularly size-driven ferroelectric-to-paraelectric phase transitions, nanopowders of ultimate particle perfection have to be stringently applied in a wide range of mean particle sizes d_m, where the correlational length is determined by relevant solid-state aspects and by no means by secondary circumstances such as lattice imperfections and impurities in the particle volume [12]. In such studies, size variation is commonly accomplished by just changing preparation conditions, first of all the reaction temperature (cf the sample series produced by co-precipitation [13]). We would be able to easily reproduce this approach by just varying the preparation temperature in our own CPP route (combined polymerization and pyrolysis of metallorganic precursors), which has so far been successfully applied to the preparation of doped perovskitic ultrafine powders ($BaTiO_3$:Mn^{2+} [14], $PbTiO_3$:Cr^{3+} [15]). However, preparing particles of smaller size at a lower temperature generally tends to reduce crystallinity and phase purity. Therefore, in order to gain a sample series of target perfection, we resorted to short-time soft milling of a parent nanopowder obtained from a tempering route at medium temperature. This approach is based on literature [16, 17] indicating that even in the case of long-time high-energy attrition milling disturbances occur at a time which is not reached in our milling procedure. In such an endeavour, the advanced liquid-precursor-based CPPl route proved to be an appropriate nanopowder source (a detailed description of the CPPl route is being prepared). As for mean particle size, our sample series falls definitely below the corresponding literature value (6 nm in the present work versus 26 nm [13]). This renders possible a direct determination of the critical size d_{cr}, which has been inferred so far from a remote data extrapolation (see, e.g., [13]). Furthermore, it is worth mentioning the rich experience which has been accumulated so far to characterize the ferroelectric state of the perovskitic nanopowders, particularly by the application of EPR spectroscopy ($BaTiO_3$:Mn^{2+} [8, 18], $PbTiO_3$:Cr^{3+} [19, 20]), and, therefore, in this work this structure-analytical tool is added to common standard methods such as scanning and transition electron microscopy (SEM, TEM), x-ray diffraction (XRD) and Raman spectroscopy (as for standard characterization, combined with dielectric measurements see e.g. [13]). Particularly in the multi-frequency EPR study of chromium-doped $PbTiO_3$,

the Cr^{3+} probe ion was found to be accommodated in the distorted TiO_6^{8-} octahedron on the near-central Ti^{4+} site (centre C1 in [20], as for an analogous analysis of defect associates occurring in $PbTiO_3$, see [21]). Therefore, prior to the intricate dielectric measurements on pellet samples with conducting surfaces, the C1 EPR features from mere EPR nanopowder measurements ensure that the milling sample series covers the size-driven transition into the cubic paraelectric phase. In the present dielectric study of size effects and size-driven transition, both with regard to particle-size and frequency ranges, we aim at going beyond the previous dielectric investigations [13], thus reconciling the different particle sizes as obtained from various techniques in the context of size effects. In particular, the coherently diffracting domain size d_{XRD} as determined by XRD is checked as a proper measure of the correlational length, and its relationship with geometrical size is of particular interest.

2. Experimental details

2.1. Synthesis of chromium-doped nanocrystalline $PbTiO_3$ powder

First of all motivated by our aim to produce nanostructured ferroelectric materials such as crystal-like nanotube arrays with the aid of a template route [22], we enhanced our former solid-precursor based CPP route [14, 15] (hereinafter referred to as CPPs) to the liquid-precursor based variant CPPl. Such an extension could not simply be achieved by just omitting an apparently dispensable drying of the liquid precursor and, instead, feeding it to the high-temperature treatment in a direct way. Rather, both solubility and reactivity aspects exist, which make these CPP versions so different that a separate description will be given to the latter CPPl variant. Here we confine ourselves to just mentioning that in the liquid-precursor case the former solid multinuclear methacrylate complex was replaced by a diacrylate compound (0.8 M in acrylic acid, with a small proportion of chromium(III) acetylacetonate added for a predominant Cr^{3+} doping of typically 5×10^{17} spins per 100 mg $PbTiO_3$ nanopowder sample). The ultrafine $PbTiO_3$ powder was obtained by the application of a specific tempering route (ambient air, heating rate 3 K min^{-1} up to 900 °C with 3 h dwell and cooling rate 5 K min^{-1}). At first, size gradation was attained by using lower tempering temperatures (700, 500, 400, 375, 350 and 320 °C in addition to 900 °C for the 'S' sample series). Alternatively, gradual reduction of the mean particle size of the 900 °C parent nanopowder was done with the aid of a planetary ball mill under soft grinding conditions (low rotation frequency 360 min^{-1}, six small ZrO_2 milling balls ⌀ 1 cm), with the milling times being 0, 5, 10, 15, 30 min; 1, 2, 3 h, 1, 2 d. Obviously, this successive milling ensures a much more systematic size gradation than mediated by the application of independent tempering temperatures. The progress is worth mentioning, which meanwhile was attained in preparing $BaTiO_3$ nanoparticles by a wet solvothermal route [23]. The particulars of the XRD patterns speak of a rather broad particle size distribution with mean particle size less than 20 nm and a co-existence of cubic and tetragonal fractions. However, size variation and doping by paramagnetic probe ions was not performed in this work.

2.2. Powder characterization

Scanning electron microscopy images were obtained at 30 keV using a JEOL JSM-6600 instrument. Electron-excited x-ray spectra (EDX) were recorded at 20 keV with a RÖNTEC EDWIN EDX system attached to the SEM (for details, cf [15]).

Transmission electron micrographs were recorded at the *caesar* research centre in Bonn with the aid of a LEO-922A, a 200 keV microscope equipped with an analytical pole-piece

($C_s = 2.2$ mm) and a LaB_6 filament. Size determination was based on the recorded pictures of several hundred nanoparticles.

Raman spectra of the $PbTiO_3$ nanopowders were taken in the frequency range between 50 and 1000 cm^{-1}, using the Bruker FT-Raman spectrometer RFS 100. The Nd:YAG laser was used as the excitation source at a power level up to 30 mW.

XRD investigations were carried out at room temperature with a powder diffractometer (Philips X Pert) in Bragg–Brentano configuration, using Cu Kα radiation. In analysing the XRD data the so-called single-line method was used, which is implemented in the WinFit V1.2 software package by Krumm [24]. The single-line method was applied to the (111) reflex. The mean particle sizes and the size distributions were determined from the second derivative of the Fourier coefficient plots. The determination of the tetragonal lattice parameters a and c was based on the (200) and (002) Bragg reflections. In doing so, their peak positions were corrected with respect to the (220) of the internal Si standard sample.

EPR measurements of the powder samples were carried out from room temperature up to 830 K, using a Varian E112 spectrometer at X-band frequency (9.5 GHz). The high-temperature cavity employed was a modified H_{101} cavity, which is water-cooled and temperature-monitored with a platinum wire resistance heating element [25]. A thermo-couple enabled *in situ* measurements which yielded a temperature gradient across the sample of about 3 K.

2.3. Dielectric measurements

Anticipating that only the milled 'T' sample series were perfectly single phase to XRD and Raman, we confined ourselves to press only 'T' powders into small pellets of 1 mm diameter and 0.9 mm thickness for the dielectric measurements. The conspicuously better mechanical pellet stability which was obtained from all the milled nanopowders as compared with the unground CPPl-prepared parent nanopowder is worth mentioning. Platinum black electrodes were sputtered on both faces of the pellet sample and afterwards cured at 850 °C for 30 min. Such a tempering readily might cause particle growth. Therefore, XRD patterns were taken prior to and after this short-time tempering. These patterns did not reveal a significant difference, testifying to size invariance. The capacitance and dielectric loss factor ($\tan\delta$) were measured at four frequencies (1 MHz, 10 MHz, 100 MHz, and 1 GHz) using a home-made set-up, which essentially is a coaxial waveguide loaded with the sample, allowing the investigation of impedance, admittance, permittivity and electric modulus of the sample over a large temperature range (300 K up to about 1000 K) at frequencies ranging from 1 MHz to the centimetre wave region. In particular, this broadband impedance spectroscopy method distinguishes between different mechanisms contributing to charge transport and polarization in materials such as solid electrolytes, ferroelectrics, semiconductors etc [26, 27].

3. Results and discussion

3.1. Structural data

The SEM micrographs in figure 1 show that even very short milling can transform the loose, CPPl-prepared nanopowder into a rather cohesive one. This also results in an enhanced mechanical pellet stability obtained from milled nanopowders as compared to those from CPPl-prepared raw powder.

A corresponding statistical analysis of the TEM micrographs (see figure 2) furnishes geometrical sizes d_{TEM} (87 and 25 nm for T1 and T9, respectively), which clearly exceed the pertinent coherently diffracting sizes d_{XRD} (29, 7 nm). At least three alternative explanations

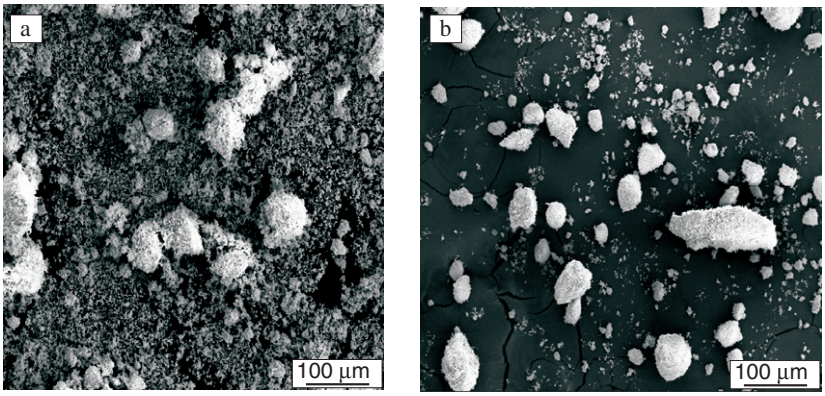

Figure 1. SEM images of chromium-doped $PbTiO_3$ nanopowders taken at low magnification (200×): as CPPl prepared (T1, d_{XRD} 29 nm; (a)) and after short-time soft post-milling (T2, 5 min, d_{XRD} 24 nm; (b)).

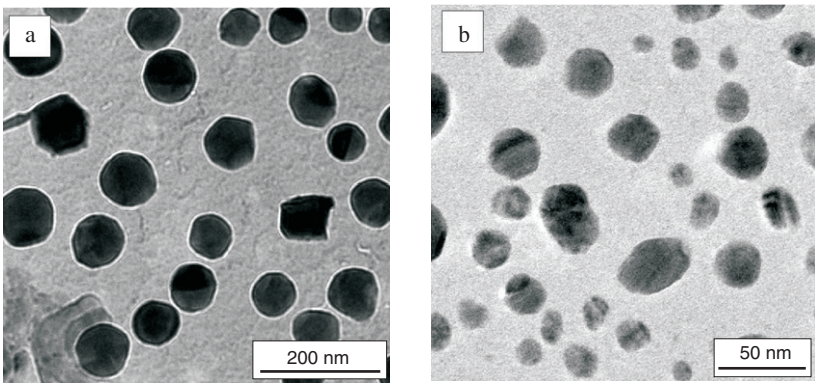

Figure 2. TEM micrographs of the as-CPPl-prepared raw nanopowder (T1, d_{TEM} 87 nm, d_{XRD} 29 nm (a)) and the long-time milled one (T10, 48 h, d_{TEM} 25 nm, d_{XRD} 6 nm (b)).

can be given to account for this apparent discrepancy between the different d_{TEM} and d_{XRD} sizes. (i) The simplest one refers to the quite different sensitivity to particle size of TEM and XRD [28]: while TEM may readily overlook particularly the small particles, the latter mainly contribute to the broadening of the XRD features. (ii) Substructures as caused by twinning or domains can both increase the geometrical size d_{TEM} and decrease the size d_{XRD} of the coherently diffracting subregion. (iii) Finally, a core–shell structure could furnish an inherent idea of such a ferroelectric particle: in particular for $BaTiO_3$ nanopowder samples some EPR features could be clearly assigned to a regular ferroelectric core, corresponding with the coherently diffracting XRD size, and an outer shell, with a tetragonality gradient occurring in the peripheral particle layer [8]. Therefore, in this study it seems quite interesting whether EPR findings can also furnish analogous evidence for a broad surface layer occurring in $PbTiO_3$ nanoparticles.

This can hardly be expected taking into account the results of [29] which brought out a surface relaxation in a $PbTiO_3$ surface layer one order of magnitude thinner than that occurring in $BaTiO_3$ particles. Once again the cohesive nature of the milled samples is worth mentioning, which strongly restricted the number of isolated single particles. Thus, the statistical basis

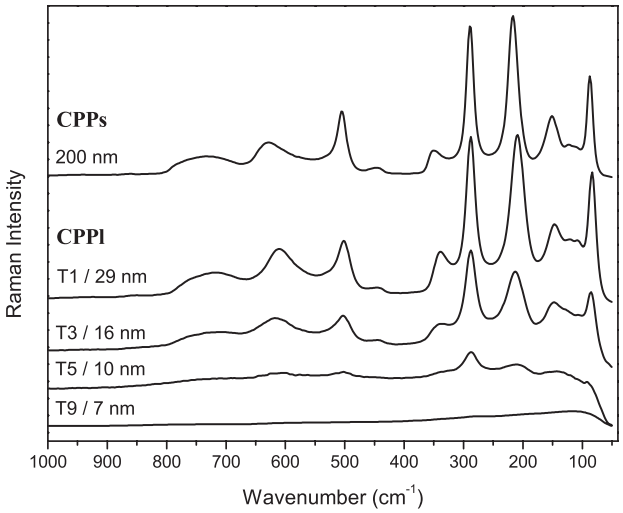

Figure 3. Raman spectra of chromium-doped $PbTiO_3$ nanopowders (from top: CPPs and CPPl prepared at 900 °C, and selected samples T3, T5 and T9 after soft milling over 10 min, 30 min and 24 h, respectively).

for deriving a size distribution from TEM micrographs proved quite poor, and with this consideration we fully resorted to XRD.

Although the same tempering temperature (900 °C) was applied, the CPPl route obviously yields powders of much smaller mean particle size than the analogous CPPs preparation. This becomes manifest in figure 3 by a corresponding broadening and downward shift of nearly all Raman lines (except for the 'silent' one at 290 cm^{-1}, cf [30]). Despite the smaller mean particle size of the CPPl-derived T1 sample, the ferroelectric activity as represented by the intense soft mode E(TO1) at about 90 cm^{-1} is comparable to that of the CPPs-derived powder, suggesting a better performance of the CPPl route. This can probably be traced back to higher reaction homogeneity, particularly in the polymerization step. As for the specific differences between the CPPs and CPPl routes, a manuscript is being prepared. With decreasing particle sizes along the 'T' milling series, the line broadenings and shifts proceed until finally all the Raman features fade away. The fading indicates that the 'T' milling series covers the size-driven tetragonal-to-cubic phase transition.

The XRD patterns in figure 4 testify to perovskitic single phase for all CPPl-derived $PbTiO_3$ 'T' samples. For the finest CPPl-derived samples, with the mean sizes decreased by an appropriate lowering of the tempering temperature, a segregated crystalline minority phase manifests itself in the pertinent XRD patterns (bottom of figure 4) by the features occurring below 30°, indicating an amorphous fraction even at further reduction of the tempering temperature (e.g. 320 °C). All the XRD peaks are considerably broadened so that the $K\alpha_1/K\alpha_2$ splitting is not detectable. By using the single-line method [24] in analysing the XRD results, narrower size distributions were found for powders with smallest mean particle sizes, with the tetragonality being reduced. Strain which might be imposed by short-time soft milling was accounted for in the XRD data processing. Nevertheless, some discord with JCPDS data remained and was qualitatively assigned to the co-existence of tetragonal and cubic proportions (see also [23]).

The size distributions in figure 5 are non-Gaussian but clearly resemble log-normal functions. Note that this feature was not obtained by a fit procedure but, rather, is the result of a

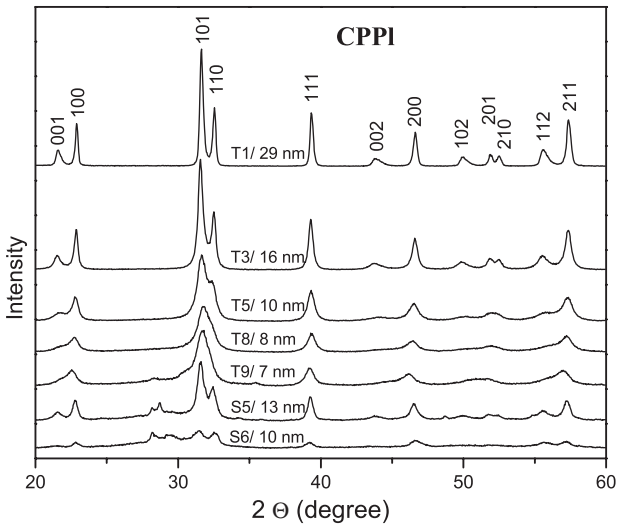

Figure 4. XRD patterns for as-CPPl-prepared raw nanopowder T1 and for selected milled samples T3, T5, T8 and T9 as well as the ultrafine 'S' powders S5 and S6 (bottom, the lowest prepared at reduced tempering temperatures 350 and 320 °C, respectively).

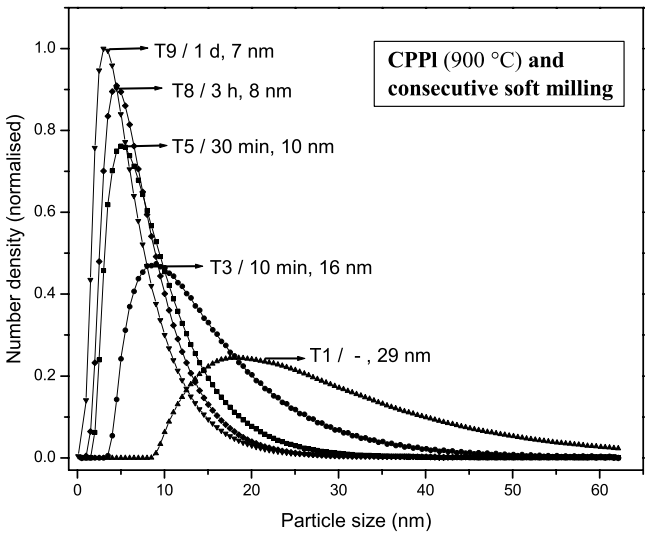

Figure 5. Normalized size number densities of CPPl-prepared chromium doped $PbTiO_3$ raw nanopowder (T1) and some selected milled 'T' samples, with milling time and resulting mean particle size d_m added to the respective powder labels T i.

straightforward calculation utilizing the single-line method [24]. Note the consistent systematic difference between T9 and T8 size distributions, which, however, is then translated in the surprisingly small d_m difference of 1 nm. Such a small d_m difference also appears significant from a methodological point of view since the statistical error in applying the single-line method under our data acquisition conditions was estimated to amount approximately 0.2 nm.

To further analyse the problem of critical size, the tetragonality parameter $(c/a - 1)$ was considered in its size dependence: the determination of the tetragonal lattice parameters a and

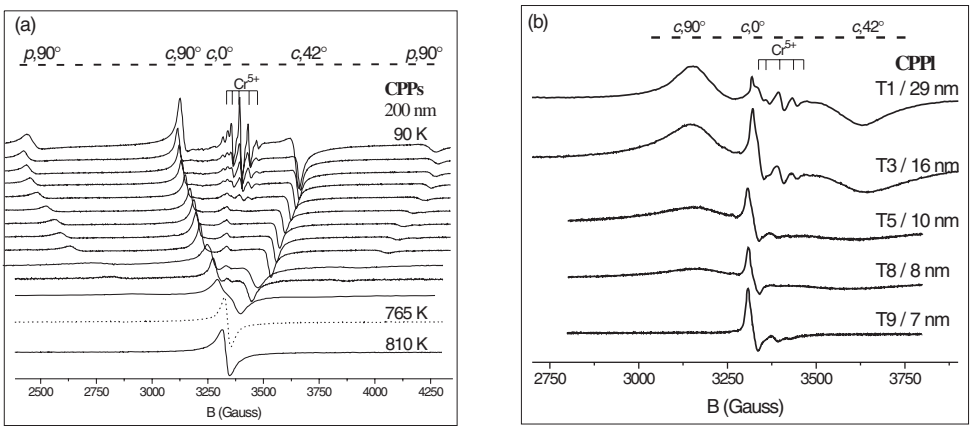

Figure 6. Changes in the chromium EPR spectra due to temperature variation (from 90 K up to 810 K in steps by 60 K (a) and as a result of size variation at room temperature (b)).

c in dependence on the mean particle size was based on the (200) and (002) Bragg reflections (for computational details, cf [15]). The size dependence of the tetragonality ($c/a - 1$) will be given later (in figure 10) in a composite of data that are also of relevance to critical size.

3.2. EPR X-band studies

To further explain the structural changes, in close correlation with size effects and size-driven phase transition in $PbTiO_3$, extensive multi-frequency EPR measurements on chromium-doped bulk systems, micro- and nanopowders were carried out [19, 20]. Four paramagnetic Cr^{3+} centres (C1, C2, C3, C4) with different axial fine structure (FS) parameters were identified, with one of them (C1) being compatible with X-band measurements on bulk [31] and microceramics [32] samples. In nanopowder samples centres other than C1 and C4 are no longer detectable. Actually, the C4 centre is in close interrelation with the axial C1 centre, since it is derived from C1 when going from the tetragonal ferroelectric to cubic paraelectric state by reducing the particle size. In the previous EPR measurements, spectrum simulation and discussion on the basis of an axial spin Hamiltonian [19], a hyperfine term could be disregarded due to the great abundance (90.5%) of $^{52,54,56}Cr$ isotopes with absent nuclear spin:

$$\hat{H} = \beta \hat{\vec{S}} \underline{\underline{g}} \vec{B} + D[\hat{S}_z^2 - \tfrac{1}{3}S(S+1)] \tag{1}$$

with $S = 3/2$ and z along the crystallographic c axis. Here we focus on X-band measurements on the C1 centre, which reveal a particularly direct and close interrelation with size effects and size-driven phase transition in $PbTiO_3$ nanopowders and particularly with pertinent dielectric measurements. Comprehensive EPR results were presented and, with regard to spectroscopic details, extensively discussed earlier [19, 20].

For delving further into the particulars of the size effects, the changes in the tetragonal X-band spectra should be analysed in greater detail. These changes reflect the approach to and finally the transition into the cubic paraelectric phase. Figure 6 demonstrates such changes both for a temperature driven (figure 6(a)) and for a size driven transition (figure 6(b)).

At first, at varying temperature a spectrum sequence was taken from a sample of relatively large mean particle size (d_{XRD} 200 nm, CPPs-prepared). Spectra recorded at a lower temperature (e.g. 90 K in figure 6(a)) reveal a multi-line spectrum in their centres, which

is to be attributed to Cr^{5+} ($S = 1/2$) ions [33]. Though being quite conspicuous, this partial spectrum is of minor importance in our context: it largely disappears at about 400 K and, hence, does not furnish any information about the temperature-driven ferroelectric-to-paraelectric phase transition. In our context the Cr^{3+} ($S = 3/2$) spectrum is of much greater relevance, because in the analogous EPR studies on $BaTiO_3$:Mn^{2+} [8, 18] the FS interaction furnished detailed information on the ferroelectric state of the host nanocrystallites. Such an FS interaction also occurs in the present case of $PbTiO_3$:Cr^{3+}, giving rise to the central FS lines (c:M_S $1/2 \leftrightarrow -1/2$) and peripheral ones (p:M_S $3/2 \leftrightarrow 1/2, -1/2 \leftrightarrow -3/2$). The specific orientations (90°, 0°, 42°) of the external magnetic B field in reference to the statistically oriented crystallographic c axis at which a statistical accumulation creates detectable FS peaks is well understood [34], and has been extensively described for the particular $PbTiO_3$:Cr^{3+} cases [20]. Most importantly, all the peak separations are determined by the tetragonal FS parameter D (proportional to D^2/B_0 and D for the c and p FS groups, respectively). Tetragonality ($c/a - 1$) decreases with growing temperature (cf also [35]). Obviously this behaviour also applies to the FS parameter D, evidencing the observed convergence of all the 'tetragonal' FS peaks, with the latter finally merging in a single 'cubic' line. However, before reaching the cubic phase, peripheral p peaks are smeared and apparently vanish due to moderate broadening of the D value distribution. Owing to quadratic dependence of the FS_c separations on D, the mergence of the FS_c peaks proceeds more rapidly and the latter remain visible until their coalescence at Curie temperature T_c. Summarizing, we can say that tetragonal peak separation and central-line intensity provide a useful picture of the approach to and transition into the cubic phase. Recalling in particular the D^2/B_0 dependence of FS_c peak separation, the intensity of the central 'cubic' line is not only built up by true cubic units but also by units revealing sufficiently weak tetragonal distortions.

Weakening the tetragonality not by temperature increase but, instead, by size reduction brings out a quite analogous picture (cf figure 6(b)): at first, the partial Cr^{5+} spectrum persists along the size series because all spectra are now recorded at room temperature. In approaching the cubic phase by size reduction, however, the Cr^{5+} spectrum also becomes secondary because of the increasing intensity domination by the Cr^{3+} 'cubic' line (attributed in preceding EPR reports [19, 20] to the C4 centre). Furthermore, while the smallest particles obviously have cut across the size-driven tetragonal-to-cubic phase transition, the larger ones still remain in the preliminary stages of this structural transmutation. At first sight, temperature- and size-dependent spectra series reveal quite analogous features; however, significant differences are worth mentioning. (i) The peripheral p, 90° peaks no longer occur and the pertinent B field range is omitted in figure 6(b). (ii) With regard to the separation of the c, 90°/c, 42° peaks, the upper T1 spectrum in figure 6(b) compares well with the spectrum taken at approximately room temperature (fifth from the top in figure 6(a)). However, the T1 spectrum obviously reveals much broader c, 90°/c, 42° peaks, then merging into a surprisingly narrow cubic line (bottom of figure 6(b)). As in the previous study of size effects on $BaTiO_3$:Mn^{2+} nanoparticles [8], the program XSophe [36] was employed to deduce the parameters of the spin Hamiltonian and their distribution from the powder spectra. This advanced simulation program is based on matrix diagonalization and the so-called Sophe scheme for partitioning the surface of the unit sphere. Repeated extensive description of the methodological approach to translate the spectral EPR features into the parameters of a core–shell particle model seems quite pointless here. Instead we just give the thickness of the distorted surface layer in $PbTiO_3$ (≈2 nm, as compared with 15 nm for $BaTiO_3$ [8]).

For the chromium-doped $PbTiO_3$ it seems interesting to observe how a consecutive temperature increase can complete the transition into the cubic phase. For a quantitative description of this consecutive process, the height I_c of the 'cubic' peak (at about 3310 G

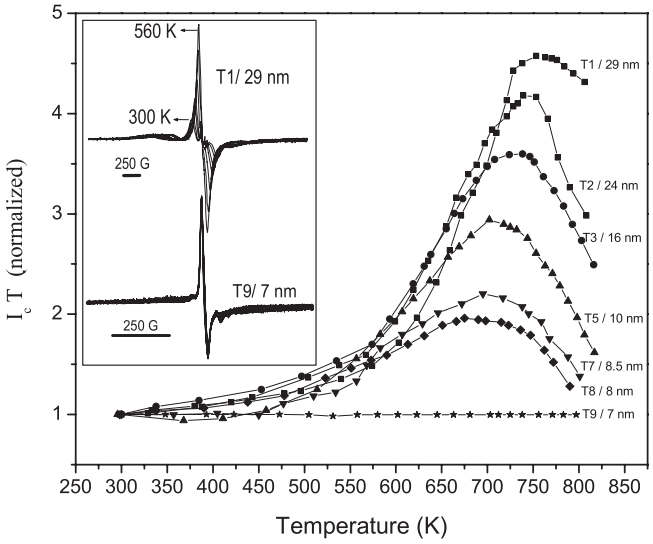

Figure 7. I_cT–T plots for CPPl-prepared nanopowder T1 and various ground 'T' samples (the inset illustrates in the upper part the strong temperature variation of central EPR features for relatively coarse T1 (29 nm) nanopowder and their extensive thermal invariability for the ultrafine T9 (7 nm) sample).

in figure 6) is used as a characteristic measure. However, having in mind the inversely proportional dependence of the EPR signal intensity on the measuring temperature [34], it appears more appropriate to base further discussion on the product I_cT instead of solely I_c. Admittedly, such an approach contains some inconsistency because (i) this field position is already occupied by the 'c, 0°' peak and (ii) not only the cubic fraction with vanishing D value makes a contribution to this particular intensity but also tetragonal fractions with small enough D parameters. Nevertheless, for the time being this route represents an optimum compromise. Furthermore, in order to adjust the intensity to the same sample amounts and detection sensitivities we normalized all I_cT–T dependences at room temperature to unity. Note that this normalization does not remove the effect of the cavity quality, which deteriorates as a result of dielectric losses through the loss angle tangent $\tan\delta$, which, as is generally known, increases in the dielectric dispersion region (cf also figure 8 in [13]). Obviously, the normalized cubic intensity I_cT increases until, in the cubic phase, all previous FS signals contribute to the 'cubic line' intensity, thus setting up a threshold characteristic running to a constant at high temperature. While in the pre-threshold region the growing $\tan\delta$ just damps the rise of the I_cT–T curve due to diminished resonator quality, it causes a descent in the originally constant region, thus finally establishing a bell-shaped characteristic, revealing a maximum at the effective phase-transition Curie temperature T_c.

The spectra in the inset of figure 7 once again illustrate the initial rise of the I_cT–T curve for the T1 (29 nm) powder. In the finer T9 powder (7 nm) sample, most of the particles have obviously cut across the size-driven phase transition into the cubic phase, hence the 'cubic' line carries almost the entire EPR intensity.

Due to normalization at room temperature to unity, the T9 curve is the lowest, largely constant line, with its straightness mainly attributable to electrical inactivity with small $\tan\delta$. In going from T8 (9 nm) to T9 (7 nm), a conspicuous abrupt decline is observed, which can be traced back to the complex intensity parentage of the 'cubic' line. Apart from this abrupt

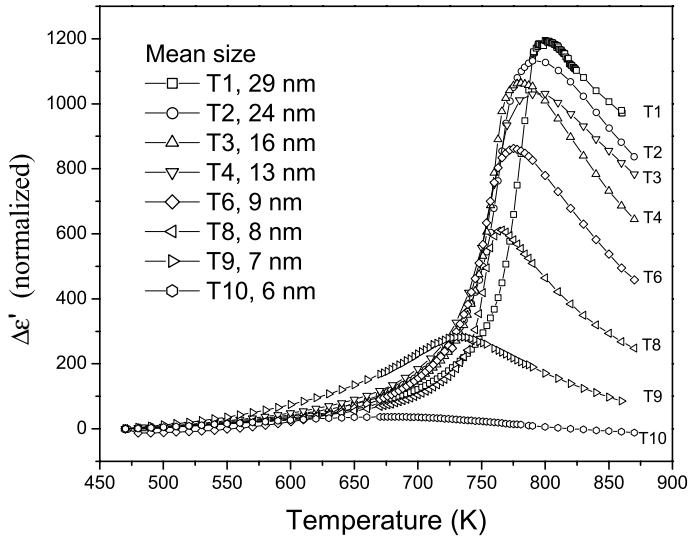

Figure 8. $\Delta\varepsilon'$–T plots taken at 1 GHz for the CPPl-prepared nanopowder T1 and post-milled 'T' samples (normalized $\Delta\varepsilon'$ data taken between room temperature and 470 K do not vary to a significant extent and, hence, were omitted here).

descent, the EPR plots in figure 7 are highly reminiscent of the ε'–T plots from dielectric literature measurements [13], motivating new intricate dielectric measurements. Such an endeavour would not constitute a mere retake, because the exceedingly large discrepancy with the literature findings [13] (e.g. T_c shifts up to 70 K as compared with 16 K and the ε' peak disappears at 6 nm instead of 26 nm) highly motivates a revisit of dielectric spectroscopy.

3.3. Dielectric spectroscopy

The temperature dependence of the dielectric response function ε' and loss ($\tan\delta$) were measured between room temperature (here shown above 470 K) and 825 K at four frequencies (1 MHz, 10 MHz, 100 MHz and 1 GHz). So far, density and geometry corrections could not remove an unreasonable scatter of low-temperature ε' data so that for low temperatures we tentatively put them to zero, thus laying stress on the shapes of the $\Delta\varepsilon'$–T plots. Considerable further data processing is necessary in order to ensure consistent presentation of the dielectric data survey. Therefore we confine ourselves to exemplify them by giving the $\Delta\varepsilon'$–T plots as taken at 1 GHz in figure 8.

Apart from the above-mentioned abrupt EPR profile decline, the close correlation between EPR 'cubic' intensity and dielectric response dependences on temperature (cp figures 7 and 8) is in fact conspicuous. Moreover, qualitative agreement with corresponding literature findings can be observed (e.g., see figure 6 in [13]). However, our dependences are represented by more regular bell-shaped profiles, vanishing at a much smaller mean particle size (d_{XRD} 6 nm, instead of 26 nm in [13]). At first, differing XRD analyses could be blamed for this discrepancy, but the same critical size as derived from our tetragonality extrapolation (6 nm) led us to assume a superior quality of our sample nanomaterial. As compared with literature findings (e.g. cf [13]), our temperature dependences in figures 7 and 8 appear quite critical with regard to trifling size alterations, indicating the very close vicinity to the likewise critical size-driven phase transition.

A preliminary simulation of our exemplifying dielectric results (cf figure 9) was done by the application of Monte Carlo calculations with a 3d Ising Hamiltonian [37]. Our preliminary

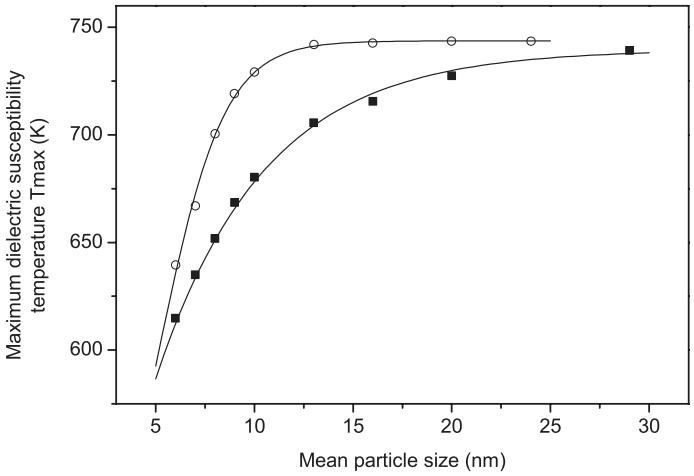

Figure 9. Comparison between dielectric susceptibility maximum values for different particle sizes obtained from Monte Carlo simulation without (filled symbols) and with (open symbols) distribution of the particle sizes.

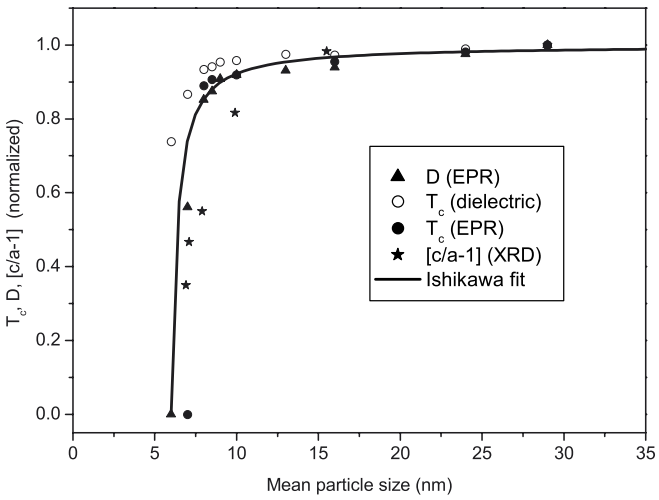

Figure 10. The values of Curie temperature, as determined by EPR, FS term value D, and quantity $(c/a - 1)$ determined by x-ray diffraction, normalized to their respective $PbTiO_3$ bulk values, as a function of mean particle size.

study of the dielectric behaviour of $PbTiO_3$ nanopowder pellets [27] clearly corroborated the significance of the particle size distributions (figure 9) in a discussion of nanopowder properties as it was demonstrated before for $BaTiO_3$ nanopowders (in particular with regard to specific heat and dielectric permittivity [38]). For a more detailed presentation of theoretical and computational dielectric studies of $PbTiO_3$ nanomaterials, the interested reader is referred to a forthcoming publication [39].

The dielectric data complement the consistent and comprehensive block of size and temperature dependent XRD, EPR and Raman data, particularly covering the critical size d_{cr}, and an Ishikawa fit [28] explicitly yields a critical size of 6 nm (figure 10).

To our best knowledge, for nanopowders such an estimation of critical particle size d_{cr} has so far only been obtained from a 'remote' extrapolation based on nanopowders with mean XRD particle sizes above 26 nm [13]. However, respective thin-film results must be taken into consideration, which also yield corresponding critical sizes below 10 nm (2.4 nm [40], 4 nm [41, 42]).

4. Conclusions

In combination with soft milling, the liquid-precursor-based CPPl route yields a target $PbTiO_3$ nanopowder basis for studying temperature- and size-driven tetragonal-to-cubic phase transitions in a direct way. Inherent in at least all high-temperature preparation procedures, relatively broad log-normal particle-size distributions determine nanopowder properties as ensemble averages. The high-quality materials basis allowed us to extend Müller's EPR-based approach to perovskitic bulk materials [9], to other such bulk systems (e.g. cf [10, 11]) and, for the first time, to nano-sized $BaTiO_3$ [8, 43] and $PbTiO_3$ systems, where the latter $PbTiO_3$ nanopowders form the subject of the present work. The latter two comparative studies brought out for the $BaTiO_3$ and $PbTiO_3$ nanopowders rather different pictures of the temperature- and size-driven ferroelectric-to-paraelectric phase transitions. Indeed, this difference can be traced back to the rather different binding conditions (strong covalency in $PbTiO_3$ owing to Pb 6s participation). In the present observation of temperature- and size-driven tetragonal-to-cubic phase transitions we were faced with a close cooperation between temperature rise and size reduction to bring about the paraelectric cubic state. In a close correspondence with dielectric measurements, the EPR spectra furnished explicit evidence that a tetragonal core and gradient surface region co-exist in a particle which is highly reminiscent of the core–shell idea for ferroelectric nanoparticles [7], where the surface boundary conditions play a major role in determining the size effects on ferroelectricity [3].

A consistent and comprehensive block of size- and temperature-dependent XRD, EPR and dielectric data particularly covers the critical size d_{cr}, and an Ishikawa fit [28] explicitly yields the small critical size of 6 nm, which is in qualitative accordance with thin-film-derived data.

In $PbTiO_3$, probably owing to the participation of the Pb 6s orbital in strong covalent binding, tetragonality proves very stable and can only be removed at a rather high temperature, extraordinarily strong reduction of particle size and for a given $PbTiO_3$ particle in an exceptionally thin surface layer. This finding is consistent with comparative estimations of surface relaxations occurring in $BaTiO_3$ and $PbTiO_3$ [29], which in turn readily explain our former finding of a broad surface layer occurring in $BaTiO_3$ [8]. In the present study, however, the main focus is set on the phenomenology of size effects, which in turn is amenable to physical interpretation by the pertinent solid-state theoreticians.

Acknowledgments

We are grateful to Dr P Morgenstern from *Umweltforschungszentrum Leipzig/Halle*, who gave great assistance in preparing the pellet samples for dielectric measurements. These investigations were financially supported by *Deutsche Forschungsgemeinschaft* within the programmes *FOR 522* and *SPP 1051* and by *Alexander von Humboldt Stiftung.*

References

[1] Akdogan E K, Leonard M R and Safari A 1999 *Handbook of Low and High Dielectric Constant Materials* vol 2, ed H S Nalwa (San Diego, CA: Academic) chapter 2

[2] Scott J F 2000 *Ferroelectric Memories* (Berlin: Springer) chapter 1.2
[3] Bratkovsky A M and Levanyuk A P 2005 *Phys. Rev. Lett.* **94** 107601
[4] Huang H, Sun C Q, Tianshu Z and Hing P 2001 *Phys. Rev.* B **63** 184112
[5] Frey M H and Payne D A 1996 *Phys. Rev.* B **54** 3158
[6] Glinchuk M D and Morozovskaya A N 2003 *Phys. Status Solidi* b **238** 81
[7] Tanaka M and Makino Y 1998 *Ferroelectr. Lett.* **24** 13
[8] Böttcher R, Klimm C, Michel D, Semmelhack H C, Völkel G, Gläsel H J and Hartmann E 2000 *Phys. Rev.* B **62** 2085
[9] Müller K A and Fayet J C 1991 *Topics in Current Physics: Structural Phase Transition II* vol 23, ed K A Müller and H Thomas (Berlin: Springer) chapter 1.4
[10] Böttcher R, Langhammer H T, Müller T and Abicht H P 2005 *J. Phys.: Condens. Matter* **17** 492
[11] Böttcher R, Erdem E, Langhammer H T, Müller T and Abicht H P 2005 *J. Phys.: Condens. Matter* **17** 2763
[12] Wada S, Suzuki T and Noma T 1995 *Japan. J. Appl. Phys.* **34** 5368
[13] Chattopadhyay S, Ayyub P, Palkar V R and Multani M 1995 *Phys. Rev.* B **52** 13177
[14] Gläsel H J, Hartmann E, Hirsch D, Böttcher R, Michel D, Hormes J and Rumpf H 1999 *J. Mater. Sci.* **34** 2319
[15] Erdem E, Böttcher R, Semmelhack H C, Gläsel H J and Hartmann E 2003 *J. Mater. Sci.* **38** 3211
[16] Leite E R, Pontes F M, Paris E C, Paskocimas C A, Lee E J H, Longo E, Picani P S, Varela J A and Mastelaro V 2000 *Adv. Mater. Opt. Electron.* **10** 235
[17] Leite E R, Santos L P S, Careno N L V, Longo E, Paskocimas C A, Varela J A, Lanciotti F, Campos C E M and Pizani P S 2001 *Appl. Phys. Lett.* **78** 2148
[18] Böttcher R, Klimm C, Völkel G, Gläsel H J and Hartmann E 1999 *Phys. Status Solidi* b **215** R3
[19] Erdem E, Böttcher R, Semmelhack H C, Gläsel H J and Hartmann E 2003 *Phys. Status Solidi* b **239** R7
[20] Erdem E, Böttcher R, Gläsel H J and Hartmann E 2005 *Magn. Res. Chem.* **43** S174
[21] Mestric H, Eichel R A, Kloss T, Laubach S, Laubach S, Schmidt P C, Schönau K A, Knapp M and Ehrenberg H 2005 *Phys. Rev.* B **71** 134109
[22] Morrison F D, Luo Y, Szafraniak I, Nagarajan V, Wehrspohn R G, Steinhart M, Wendorff J H, Zakharov N D, Mishina E D, Vorotilov K A, Nakabayashi S, Ramesh R and Scott J F 2003 *Rev. Adv. Mater. Sci.* **4** 114
[23] Kim C, Park J, Moon B, Seo H, Choi B, Yeo K, Chung S, Son S and Kim J 2005 *J. Korean Phys. Soc.* **46** 308
[24] Krumm S 1996 *Mater. Sci. Forum* **228–231** 183
[25] Milsch B and Heinhold D 1990 *Exp. Tech. Phys.* **38** 341
[26] Sobiestianskas R, Dindune A, Kanepe Z, Ronis J, Kepionis A, Kazakevieius E and Orliukas A 2000 *Mater. Sci. Eng.* B **76** 184
[27] Grigalaitis R, Banys J, Lapinskas S, Erdem E, Böttcher R, Gläsel H J and Hartmann E 2005 *Proc. III. Int. Mater. Symp. (Lisbon)* p 355
[28] Ishikawa K, Yoshikawa K and Okada N 1988 *Phys. Rev.* B **37** 5822
[29] Ishikawa K and Uemori T 1999 *Phys. Rev.* B **60** 11841
[30] Ishikawa K, Nomura T, Okada N and Takada K 1996 *Japan. J. Appl. Phys.* **35** 5196
[31] Laguta V V, Antimirova T V, Glinchuk M D, Bykov J P, Rosa J, Zaritskii M and Jastrabik L 1997 *J. Phys.: Condens. Matter* **9** 10041
[32] Heidler R, Windsch W, Böttcher R and Klimm C 1990 *Chem. Phys. Lett.* **175** 55
[33] Böttcher R, Brunner W, Milsch B, Völkel G and Kirillov S 1986 *Chem. Phys. Lett.* **129** 546
[34] Weil J A, Bolton J R and Wertz J E 1994 *Electron Paramagnetic Resonance—Elementary Theory and Practical Applications* (New York: Wiley) pp 94, 493–7
[35] Kleemann W, Schäfer F J and Rytz D 1986 *Phys. Rev.* B **34** 7873
[36] Heichel M, Höfer P, Kamlowski A, Griffin M, Muys A, Noble C, Wang D, Hanson G R, Eldershaw C, Gates K E and Burrage K 2000 *Bruker Rep.* **148** 6
[37] Binder K and Heermann D W 2002 *Monte Carlo Simulation in Statistical Physics* (Heidelberg: Springer) chapter 2
[38] Glinchuk M D and Bykov P I 2004 *J. Phys.: Condens. Matter* **16** 6779
[39] Grigalaitis R, Banys J, Lapinskas S, Erdem E, Böttcher R, Gläsel H J and Hartmann E 2006 *Mater. Sci. Forum* **514–516** 235–9
[40] Chandra P, Dawber M, Littlewood P B and Scott J F 2004 *Ferroelectrics* **313** 7
[41] Ahn C H, Triscone J M and Mannhart J 2003 *Nature* **424** 1015
[42] Junquera J and Ghosez P 2003 *Nature* **423** 506
[43] Glinchuk M D, Kondakova I V, Laguta V V, Slipenyuk A M, Bykov I P, Ragulya A V and Klimenko V P 2005 *Acta Phys. Pol.* A **108** 47